

## Effects of Coarsely Resolved and Temporally Interpolated Lateral Boundary Conditions on the Dispersion of Limited-Area Ensemble Forecasts

PAUL NUTTER\*

*School of Meteorology, and Center for Analysis and Prediction of Storms, University of Oklahoma, Norman, Oklahoma*

DAVID STENSRUD

*National Severe Storms Laboratory, Norman, Oklahoma*

MING XUE

*School of Meteorology, and Center for Analysis and Prediction of Storms, University of Oklahoma, Norman, Oklahoma*

(Manuscript received 7 August 2003, in final form 26 January 2004)

### ABSTRACT

This work examines the impact of coarsely resolved and temporally interpolated lateral boundary conditions (LBCs) on the dispersion of limited-area-model (LAM) ensemble forecasts. An expression is developed that links error variance spectra to ensemble spread while accounting for spatial and ensemble mean errors. The balances required by this expression are used to show that LBC constraints on small-scale error variance growth are sufficient to help cause underdispersive LAM ensemble simulations. The hypothesis is tested in a controlled and efficient manner using a modified barotropic channel model. Ten-member ensemble simulations are produced over many cases on a “global” periodic channel domain and each of four smaller nested LAM domains. Lateral boundary effects are specifically isolated since all simulations are perfect except for initial condition perturbations and the use of coarsely resolved and/or temporally interpolated “one-way” LBCs. This configuration excludes other analysis and external model system errors that are not caused directly by the implementation of LBCs.

Statistical results accumulated over 100 independent cases demonstrate that LAM ensembles remain underdispersive even when using a complete set of LBCs from an external ensemble forecast. The small-scale constraints on error growth are present in any modeling system using coarsely resolved or temporally interpolated one-way LBC forcing. Although not tested here, similar limitations may apply to global variable-resolution models because of insufficient small-scale variance outside the perimeter of higher-resolution subdomains. The results of this work suggest the need to apply statistically consistent, small-scale LBC perturbations at every time step throughout the LAM simulations.

### 1. Introduction

It is well known that skill in predicting future atmospheric motions is limited due to the natural growth of errors resulting from imperfect observations and analyses (Thompson 1957; Lorenz 1963). More precisely, accepted predictability theories ascribe an inverse relationship between wavenumber and time limits of predictive skill (e.g., Lorenz 1969a). In apparent contradiction to these theories, several predictability experiments using limited-area models (LAMs) report little or no error growth resulting from perturbed initial condi-

tions (Paegle et al. 1997, and references therein). Attempts to explain these seemingly optimistic results have focused either on enhanced local forcing (e.g., topography or surface inhomogeneities) or on the errors introduced by the use of “one-way” lateral boundary conditions (LBCs). The latter effect is favored in the literature and is the subject of the current work. While previous studies have considered LBC constraints on error growth for individual LAM forecasts (reviewed below), this work emphasizes the impact of coarsely resolved and temporally interpolated LBCs on the dispersion of LAM ensemble forecasts.

Results from dynamical, or “classic,” predictability experiments show that any small error in the initial conditions (ICs) will grow and spread to other wavenumbers via upscale and downscale transport of energy (e.g., Charney et al. 1966; Smagorinsky 1969; Lorenz 1982; Baumhefner 1984; Dalcher and Kalnay 1987; Reynolds et al. 1994; and many others). Error growth rate esti-

---

\* Current affiliation: Cooperative Institute for Mesoscale Meteorological Studies, University of Oklahoma, Norman, Oklahoma.

---

*Corresponding author address:* Dr. Paul Nutter, CIMMS, University of Oklahoma, 100 E. Boyd St., Rm. 1110, Norman, OK 73019.  
E-mail: Paul.Nutter@unco.edu

mates from such studies are model dependent and are limited to relatively larger scales because of practical constraints on model resolution. Alternatively, predictability estimates may be obtained theoretically by evaluating the spectral distribution of errors following a manipulation of simplified equations of atmospheric motion (Lorenz 1969b,c; Leith 1971; Leith and Kraichnan 1972; Boer 1984; Lilly 1984; Thompson 1984; and others). Error growth rate estimates from these studies are not limited in scale, but do not adequately represent the full range of atmospheric instabilities. In spite of their different approaches, the main conclusion from either type of study is that small-scale errors are expected to grow most rapidly so that short wavelengths have short predictability limits. This behavior is expected regardless of whether errors originated from IC uncertainty or from numerical model deficiencies (Lorenz 1984; Dalcher and Kalnay 1987; Reynolds et al. 1994; Toth et al. 1997; Harrison et al. 1999; Orrell et al. 2001).

The predictability theories outlined above have led some to a rather pessimistic viewpoint of mesoscale predictability because of the expectation that error growth is more rapid at smaller scales (Tennekes 1978). However, Lilly (1984) and Anthes et al. (1985) represent those who proffer the alternative hypothesis that enhanced localized forcing and highly organized circulations may help slow error growth rates. An obvious approach for testing these conflicting hypotheses at smaller scales is to use limited-area models because they can obtain highly resolved solutions with reasonable computational expense.

Anthes et al. (1985) and Anthes (1986) were among the first to conduct predictability experiments using LAMs. In contrast to results from earlier studies using global models, they reported little or no error growth resulting from small variations in the initial conditions. Furthermore, they showed that their simulations were more sensitive to variations in the LBCs than to the ICs. Errico and Baumhefner (1987) followed on this work, reporting that IC error growth is restricted in a mesoscale model due to dissipation of errors through gravity waves, the "sweeping out" of errors by the LBCs, and numerical dissipation of subgrid-scale errors. Anthes et al. (1989) reported similar results, stating that ". . . the quality of the LBC is more important than any other factor tested in the temporal evolution of model errors." Vukicevic and Paegle (1989) and Vukicevic and Errico (1990) contributed further by demonstrating that one-way LBC constraints on error growth are more pronounced as the size of the regional domain decreased. They showed that unperturbed LBC information crossed the domain more quickly on smaller domains and had less time to interact with amplifying IC errors.

While LBCs are now recognized as an artificial constraint on mesoscale error growth (Warner et al. 1997), other studies have emphasized the possibility for enhanced predictability due to stronger dynamical forcing

from the lower boundary. For example, sensitivity to small-scale IC errors could be small in cases where topographic forcing is dominant (Van Tuyl and Errico 1989; Vukicevic and Errico 1990). Warner et al. (1989) also found that error growth over the interior of the mesoscale domain decreased most rapidly during the first eight forecast hours, before lateral boundary errors could have propagated into the area tested. They suggested that this decrease in error was due to geostrophic adjustment, surface forcing, and redevelopment of smoothed features. These results indicate that simple turbulence models of error growth that anticipate the most rapid error growth at small scales may not fully explain actual error growth behaviors.

The difficulties in obtaining predictability estimates using LAMs also cause problems for short-range ensemble forecasting (SREF). Specifically, recent SREF experiments have shown that the ensembles are underdispersive (Hamill and Colucci 1997; Du and Tracton 1999; Hou et al. 2001; Wandishin et al. 2001). That is, the verifying analysis often does not fall within the range of possible solutions forecast by the ensemble. Du and Tracton (1999) found that a regional ensemble with a larger domain produces greater spread than does an ensemble with a smaller domain, especially for those variables that were perturbed in the ICs. Furthermore, they found that the contribution to ensemble spread increases with time from LBC perturbations and decreases with time from the IC perturbations. Similarly, Hou et al. (2001) showed that ensemble spread grows quickly for a SREF system configured so that each member forecast has a unique LBC; a SREF system configured so that each member has the same LBC had a slower rate of ensemble dispersion. These and other similar results (Hamill and Colucci 1997; Hou et al. 2001) demonstrate that, with time, LAM ensemble spread becomes increasingly determined by the spread in the LBCs as high-frequency components are "swept" from the LAM domain.

Results from the studies reviewed above do not indicate with certainty the relative importance of the different effects contributing to artificial constraints on error growth rates and ensemble dispersion in LAMs. The evidence tends to favor LBC effects, but other mechanisms such as enhanced local forcing, physical parameterizations, or poorly specified initial perturbations have not been eliminated from consideration. To help focus and control the research problem, we begin with the following assumptions. First, it is assumed that natural error growth at large scales is (or can be) stated accurately using global model forecasts. This is important because error growth at scales larger than the LAM domain is controlled exclusively through the LBCs (Laprise 2003). Second, we assume that error growth rates at small scales in LAMs should behave the same as calculated for global models operating at equivalent resolution. Specifically, we favor the "pessimistic" viewpoint that errors grow most rapidly at small scales.

Third, we assume that LAM ensembles should produce the same spread as global ensembles when operated with the same model and initial perturbations. That is, LBCs should not artificially constrain LAM ensemble spread.

These stated assumptions allow a more complete and controlled investigation of the impact of coarsely resolved LBCs on error growth rates and ensemble dispersion in LAMs using a simplified and idealized “perfect” model configuration. Following a “big brother” methodology (Vukicevic and Paegle 1989; Laprise et al. 2000; De Elía and Laprise 2002; Denis et al. 2002b, 2003), an appropriate high-resolution model is used to construct a known truth on a global, or laterally unbounded domain. Then, using the same model operating with the same resolution, simulations are run on regional domains with LBCs given by a subset of the control fields. With this approach, the only unavoidable source of model errors are those introduced by the use of the one-way LBCs. Additional errors may be introduced by perturbing the ICs, or by filtering the control fields to remove small-scale information from the LBCs. If the evolution of the large-scale fields is specified using perfect LBCs, then differences between small-scale error growth on the regional and global domains may be attributed directly to LBC effects. In this study, we seek to identify LAM constraints on error growth rates and ensemble dispersion caused specifically by the use of coarsely resolved and/or temporally interpolated LBCs on different-sized domains.

A statistical framework for evaluating output from the global and LAM ensembles is presented in section 2. The simplified model used for this research is described in section 3. In section 4, statistical results from a “global” ensemble using the simplified model are shown to behave qualitatively in the same way expected from the theoretical and experimental results described above. This result allows generalization of the findings in sections 5 and 6 that discuss the effect of coarsely resolved and temporally interpolated LBCs on the dispersion of LAM ensembles. The work is summarized in section 7.

## 2. Ensemble statistics

Statistical measures of ensemble performance are introduced in this section. These measures include the ensemble mean square error, dispersion, and total error variance. The total error variance has equivalent vector (spatial) and spectral representations, allowing decompositions of error variance into contributions by different scales of motion. An expression is derived that provides a direct link between ensemble dispersion and the scale decomposition of error variance. This expression allows one to measure how ensemble dispersion is affected by error growth at individual scales of motion.

### a. Notation

Spatial and ensemble means are described here using notation inspired largely by Stephenson and Doblas-Reyes (2000). Suppose  $\mathbf{x}_i$  is a vector defined on a  $p$ -element grid, obtained by aligning in a column the grid points of two- or three-dimensional fields of forecasts or analyses contained in an  $N$ -member ensemble, where  $i = 1, \dots, N$ . The ensemble mean (also a  $p$ -element vector) is defined as

$$\bar{\mathbf{x}} = \frac{1}{N} \sum_{i=1}^N \mathbf{x}_i. \quad (1)$$

The scalar spatial mean for the  $i$ th ensemble member is given by

$$\langle \mathbf{x}_i \rangle = \frac{1}{p} \sum_{k=1}^p x_{i,k} = \frac{1}{p} \mathbf{1} \cdot \mathbf{x}_i, \quad (2)$$

where  $\mathbf{1}$  is a  $p$ -element vector of ones. A useful norm representing the average sum of squares (dot product) over the grid is

$$\|\mathbf{x}_i\|^2 = \frac{1}{p} \mathbf{x}_i \cdot \mathbf{x}_i = \frac{1}{p} \sum_{k=1}^p x_{i,k}^2. \quad (3)$$

It is helpful to note for later derivations that  $\|\mathbf{1}\|^2 = (1/p)\mathbf{1} \cdot \mathbf{1} = 1$ . Note that an appropriate area-weighting factor should be applied in these definitions when representing fields projected on a conformal latitude–longitude grid (Stephenson and Doblas-Reyes 2000). We do not include such a factor here because the model used for this work is constructed using a strictly Cartesian grid.

Henceforth, let  $\mathbf{f}_i(t)$  denote individual forecast vectors from the ensemble, and  $\mathbf{a}(t)$  represent the analysis vector corresponding to each forecast. These notations and the statistical measures they help define below are applicable for gridded fields on both global and limited-area domains unless specified otherwise.

### b. Ensemble MSE and dispersion

One of the most basic measures of ensemble forecast accuracy is the ensemble mean-square error (MSE),

$$S^2 = \frac{1}{N} \sum_{i=1}^N \|\mathbf{f}_i - \mathbf{a}\|^2. \quad (4)$$

It is useful to manipulate  $S^2$  by adding and subtracting the ensemble mean forecast  $\bar{\mathbf{f}}$  and analysis  $\mathbf{a}$  with the result that

$$S^2 = \frac{1}{N} \sum_{i=1}^N \|\mathbf{f}_i - \bar{\mathbf{f}}\|^2 + \|\bar{\mathbf{f}} - \mathbf{a}\|^2. \quad (5)$$

Note that cross-product terms vanish after taking the ensemble average during expansion of the norm. Let  $D^2 = 1/N \sum_{i=1}^N \|\mathbf{f}_i - \bar{\mathbf{f}}\|^2$  define the ensemble dispersion, or spread, so that (5) becomes

$$S^2 = D^2 + \|\bar{\mathbf{f}} - \mathbf{a}\|^2. \quad (6)$$

These results show that the squared error of the ensemble mean  $\|\bar{\mathbf{f}} - \mathbf{a}\|^2$  is less than the ensemble mean square error  $S^2$  because ensemble dispersion  $D^2$  allows unpredictable components of the flow to be averaged out in the ensemble mean (Leith 1974; Stephenson and Doblas-Reyes 2000).

### c. Total biased error variance

Ensemble MSE and dispersion are commonly used measures of ensemble accuracy, but do not provide for a direct scale decomposition of error growth. The desired scale decomposition is provided by the total biased error variance,  $\sigma^2$ , because it has equivalent vector and spectral definitions. In vector form,  $\sigma^2$  is defined as an ensemble average error variance relative to a spatial mean so that

$$\sigma^2 = \frac{1}{N} \sum_{i=1}^N \|(\mathbf{f}_i - \mathbf{a}) - \langle \mathbf{f}_i - \mathbf{a} \rangle \mathbf{1}\|^2. \quad (7)$$

The unity vector multiplies the scalar spatial mean to enable vector subtraction and to allow proper application of the norm notation.

The total biased error variance ( $\sigma^2$ ) may be obtained equivalently in spectral form as (Errico 1985)

$$\sigma^2 = \frac{1}{N} \sum_{i=1}^N \sum_{\kappa=1}^{K-1} 2|F_i(\kappa)|^2, \quad (8)$$

where  $F_i(\kappa)$  is the discrete Fourier transform of  $\mathbf{f}_i - \mathbf{a}$  and  $\kappa = 1, \dots, K-1$  are the set of Nyquist resolved wavenumbers on the grid (Errico 1985). In this form, error variances may be computed individually for specific wavenumbers, or accumulated over a range of scales.

One-dimensional spectra are obtained from the two-dimensional fields using the procedure described by Errico (1985). Specifically, linear trends are first removed from each row and column of the two-dimensional grid. Then variance spectra are obtained by summing the magnitude of Fourier coefficients within annular rings in wavenumber space. Although universally valid, the variance decomposition (8) is an approximation when applied to nonperiodic fields on limited-area domains (Errico 1985, 1987; Denis et al. 2002a). Additional details on the decomposition are given by Errico (1985) and Nutter (2003).

The total biased error variance  $\sigma^2$  can be related to  $S^2$  as follows. First, multiply the grid average for each forecast  $\langle \mathbf{f}_i \rangle$  and analysis  $\langle \mathbf{a} \rangle$  by the unity vector  $\mathbf{1}$ . Next, add and subtract the resulting vectors within (4) and manipulate to obtain

$$\begin{aligned} S^2 &= \frac{1}{N} \sum_{i=1}^N \|(\mathbf{f}_i - \mathbf{a}) - \langle \mathbf{f}_i - \mathbf{a} \rangle \mathbf{1}\|^2 \\ &+ \frac{1}{N} \sum_{i=1}^N (\langle \mathbf{f}_i \rangle - \langle \mathbf{a} \rangle)^2. \end{aligned} \quad (9)$$

The combination of (7) and (9) reveals that

$$\sigma^2 = S^2 - \frac{1}{N} \sum_{i=1}^N (\langle \mathbf{f}_i \rangle - \langle \mathbf{a} \rangle)^2. \quad (10)$$

Hence, the total biased error variance is the ensemble MSE reduced by the ensemble mean square spatial error. The spatial error (bias) term becomes negligible on large or laterally unbounded domains so that the ensemble mean square error can be used as an approximation for the total biased error variance.

### d. Scale decomposition of dispersion

A key aspect of this work is to study the impact of scale-deficient lateral boundary conditions on LAM ensemble dispersion. To study this effect as a function of wavelength, an expression is needed that links ensemble dispersion to the spectral decomposition of total error variance. Such an expression is obtained directly from (6) and (10) so that

$$D^2 = \sigma^2 + \frac{1}{N} \sum_{i=1}^N (\langle \mathbf{f}_i \rangle - \langle \mathbf{a} \rangle)^2 - \|\bar{\mathbf{f}} - \mathbf{a}\|^2. \quad (11)$$

Using the spectral variance (8), Eq. (11) shows that ensemble dispersion is determined by the accumulated contributions to error variance at all resolved wavelengths, the ensemble mean-square spatial error, and a reduction from the squared error of the ensemble mean. Hence, a loss of error variance at any scale constrains ensemble dispersion unless offset by changes in the bias terms. This expression is used later to evaluate the impact of LBCs on ensemble dispersion by comparing the magnitudes of each term obtained for both global and LAM simulations.

The latter two terms in (11) cannot be decomposed in a simple way to reveal their contributions to  $D^2$  at different scales. However, if these terms are nearly the same for both global and LAM simulations, then their contributions to  $D^2$  are negated under comparison. Under this condition, the direct spectral relation between error variance and ensemble dispersion is maintained. In the perfect model simulations conducted for this work, the ensembles are unbiased and the spatial error term is negligible on large domains. However, on small domains, the spectral calculation of ensemble dispersion could become distorted because of phase errors introduced by upscale perturbation growth. The ensemble bias term could become large in practical application due to model deficiencies. However, ensembles can be calibrated to remove such biases (Hamill and Colucci 1997; Hamill 2001).

### e. Normalized error variances

The basic statistics defined above are simple measures of accuracy that do not account for skill relative to a standard benchmark. Since the theoretical upper bound for  $S^2$  and  $\sigma^2$  at error saturation is twice the climate variance of analyses (Leith 1974; Nutter 2003), the cli-

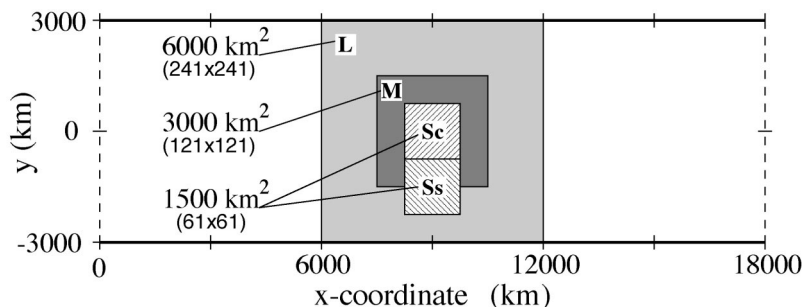


FIG. 1. Configuration of grids nested within the zonally periodic channel domain labeled L (large), M (medium), Sc (small, center), and Ss (small, south). Each grid is nested only once within the full channel grid; there are no “multiple nests.” The dimensions and number of points defining each grid are as indicated.

matological variance provides a natural standard of forecast skill.

Let  $F_{a_j}(\kappa)$  be the coefficients obtained from the discrete Fourier transform of the analysis field  $\mathbf{a}_j$ , where  $j = 1, \dots, M$ , and  $M$  denotes the number of independent cases. Then, following Eq. (8), the fraction of total variance contributed by wavenumber(s)  $k_1$  through  $k_2$  ( $1 \leq k_1 \leq k_2 \leq K - 1$ ), averaged over all  $M$  cases, is determined using

$$\tilde{\eta}_a(\kappa) = \frac{\frac{1}{M} \sum_{j=1}^M \frac{1}{N} \sum_{i=1}^N \sum_{\kappa=k_1}^{k_2} 2|F_{ij}(\kappa)|^2}{\frac{1}{M} \sum_{j=1}^M \sum_{\kappa=k_1}^{k_2} 2|F_{a_j}(\kappa)|^2}. \quad (12)$$

The normalization applies equally to all wavenumbers and has a theoretical maximum value of 2.

### 3. Model description and its configurations

Numerical experiments are conducted using a single-level parameterized potential vorticity (PPV) channel model configured to isolate the effects of LBCs on LAM ensemble dispersion while avoiding analysis and model system errors. Although simplified, the PPV model remains nonlinear, dispersive, and sensitive to IC perturbations.

The PPV model is based on the quasigeostrophic potential vorticity equation. Minimal treatment of baroclinic effects requires a multilevel modeling system. However, Holton (1979, section 8.4.2) suggests that the first-order effects of vorticity stretching may be included in a single-level barotropic model by parameterizing the baroclinic component of quasigeostrophic potential vorticity in terms of the Rossby radius of deformation.

Let  $\xi \equiv \zeta - \lambda^2 \psi$  define the parameterized potential vorticity, where  $\zeta$  denotes relative vorticity,  $\psi$  is the streamfunction, and  $\lambda$  is the inverse of the Rossby radius of deformation, specified so that  $\lambda^{-1} = 1414.2$  km. If we apply this approximation to the quasigeostrophic potential vorticity equation and introduce a fourth-order

numerical diffusion term having an eddy diffusion coefficient  $\nu$ , we obtain the PPV model

$$\frac{\partial \xi}{\partial t} = \frac{\partial \psi}{\partial y} \frac{\partial \xi}{\partial x} - \frac{\partial \psi}{\partial x} \left( \frac{\partial \xi}{\partial y} + \beta \right) - \nu \nabla^4 \xi, \quad (13)$$

where  $\beta$  is the meridional gradient of earth’s vorticity evaluated at 45°N latitude.

The PPV model (13) is solved numerically on a uniform mesh with a grid spacing of  $(\Delta x, \Delta y) = 25$  km and a time step of  $\Delta t = 7.5$  min. The eddy diffusion coefficient is specified as  $\nu = 1.0 \times 10^{12} \text{ m}^4 \text{ s}^{-1}$  to yield an  $e$ -folding dissipation time of about four time steps for the shortest resolved wavelength (Xue 2000). Spatial derivatives are evaluated using second-order centered finite differences, while temporal integration is conducted using the second-order, two-step leapfrog-trapezoidal scheme (e.g., Durran 1999). An Arakawa (1966) Jacobian is applied to conserve domain-integrated enstrophy and kinetic energy. A complete description of the model and its numerical configuration is given by Nutter (2003).

PPV model simulations are run with both “global” and limited-domain simulations (Fig. 1). The global model configuration operates on a periodic channel domain. Impermeable, free-slip north and south boundaries enforce zero vorticity and constant streamfunction using specified Dirichlet boundary conditions. Periodic boundary conditions along the zonal (east/west) direction allow uninterrupted flow so that  $\psi(x + L_x, y) = \psi(x, y)$  and  $\xi(x + L_x, y) = \xi(x, y)$ . Initial conditions are obtained on the periodic channel domain by adding random perturbations to an analytic shear flow, integrating the model forward 20 days to allow the flow to destabilize, then resetting time to zero (Nutter 2003). Integrations are restarted and proceed for another 15 days to produce model-generated “truth” states. All global and LAM simulations have the same time step and grid spacing as the model-generated truth runs to remove the impact of numerical discretization errors.

The LAM simulations are configured using one-way

Dirichlet boundary conditions for  $\psi$  and  $\xi$  obtained from subsets of the global model simulations (Fig. 1). The one-way LBC scheme in the LAM simulations applies a seven-point peripheral wave-absorbing zone (Davies 1976, 1983). This method is selected because of its simplicity and common use in many current operational and research model configurations. Baumhefner and Perkey (1982) explored the significance of boundary errors in LAMs and found that differences in simulations using two different LBC formulations was small compared to the error generated by inaccurate boundary forcing. Therefore, the particular choice of LBC scheme is not expected to change the outcome of the experiments conducted here.

The PPV model used herein has the advantage of simplicity but transfers energy more slowly across the spectrum compared to true atmospheric flows. The PPV model lacks forcing due to factors such as moist physics, radiation, thermal gradients, or interaction with the lower boundary. Therefore, the climate variance for the PPV model is not stationary, but drifts lower with time. For these reasons, climate variances are computed as a function of time over 100 independent truth cases and used to normalize all error variances presented in later sections. In spite of these limitations, normalized error growth behaviors presented below are at least qualitatively consistent with results obtained from more realistic models.

#### 4. Statistics of “global” model ensemble

Ensemble simulations using the global periodic channel configuration are needed to establish benchmark error growth characteristics for the PPV model.

##### a. Production of ensembles

The model-generated climatology of 100 independent cases is used to obtain ICs and perturbations for ensembles following the method used by Schubert and Suarez (1989). Specifically, two unique states are randomly selected from the model’s set of climatological states. Perturbations are then formed by scaling the difference between the two samples by a factor of 0.10. Finally, the perturbation field is added to an IC field represented by another climatological state. This perturbation procedure is repeated 10 times for a given initial field to create the starting conditions for 10-member ensemble simulations. One hundred independent 10-member ensemble simulations are constructed by assigning perturbations to ICs given by each of the available climatological cases.

The perturbation method used here is rather simplistic, but it effectively creates ensemble dispersion by introducing errors that grow through nonlinear model dynamics. Ensemble dispersion was defined previously as a scalar statistic following Eq. (5). A slight alteration to this definition yields a vector form of dispersion,

denoted  $\mathbf{d}^2$ , that may be viewed as a two-dimensional contour plot. Specifically, at each grid point  $p$  in the domain, field dispersion for an  $N$ -member ensemble is given by

$$\mathbf{d}_p^2 = \frac{1}{N} \sum_{i=1}^N (\mathbf{f}_{p,i} - \overline{\mathbf{f}}_p)^2. \quad (14)$$

Figure 2 shows the results of this calculation for the example ensemble case. Growth of dispersion for the streamfunction is notably slow. This result is expected from any barotropic model, especially given synoptic-scale perturbations. On the other hand, vorticity dispersion grows very quickly in the first two days, and gradually organizes with time toward larger scales. Dispersion varies widely in space and time for both variables, a characteristic that is common to all ensemble systems. As reported in Nutter (2003), all statistics are evaluated in terms of vorticity since its error growth is more active at small scales than for other variables.

##### b. Normalized error variance spectra

Vorticity error growth characteristics for the “global” model configuration are considered first in terms of their normalized error variance spectra [Eq. (12)]. The results shown in Fig. 3 are calculated hourly for each 10-member ensemble, then averaged over all 100 independent cases. Although simulations are conducted on the full periodic channel domain, variance spectra are calculated separately for each of the four subdomains outlined previously in Fig. 1. These calculations enable direct comparisons to results from LAM simulations presented in later sections.

Results shown in Fig. 3 reveal that error growth due to initial perturbations is most rapid at short wavelengths. Error variance contributions at wavelengths  $50 \leq \lambda \leq 250$  km approach the expected maximum value of 2 within about 48 h on all subdomains. In general, error growth rates become progressively slower at longer wavelengths. The simulations are not run long enough to allow error saturation at scales larger than about 1000 km. However, this is not considered important since the model experiments are designed to investigate impacts of LBC constraints on small-scale error growth. Error growth rates for the PPV model are slower than those found in primitive equation models, but behave in a manner that is qualitatively consistent with theory and observations. Hence, results from these numerical experiments may be generalized in a qualitative manner.

An interesting behavior is seen in the 1500-km wavelength band when compared on the different subdomains. On the large and medium grids (Figs. 3a,b), the normalized error variance for this band reaches 1.5 by the end of the simulations. Corresponding values are about 1.2 on the small, centered grid and 1.8 on the small, southern grid (Figs. 3c,d). This result suggests that synoptic-scale waves are less predictable when dis-

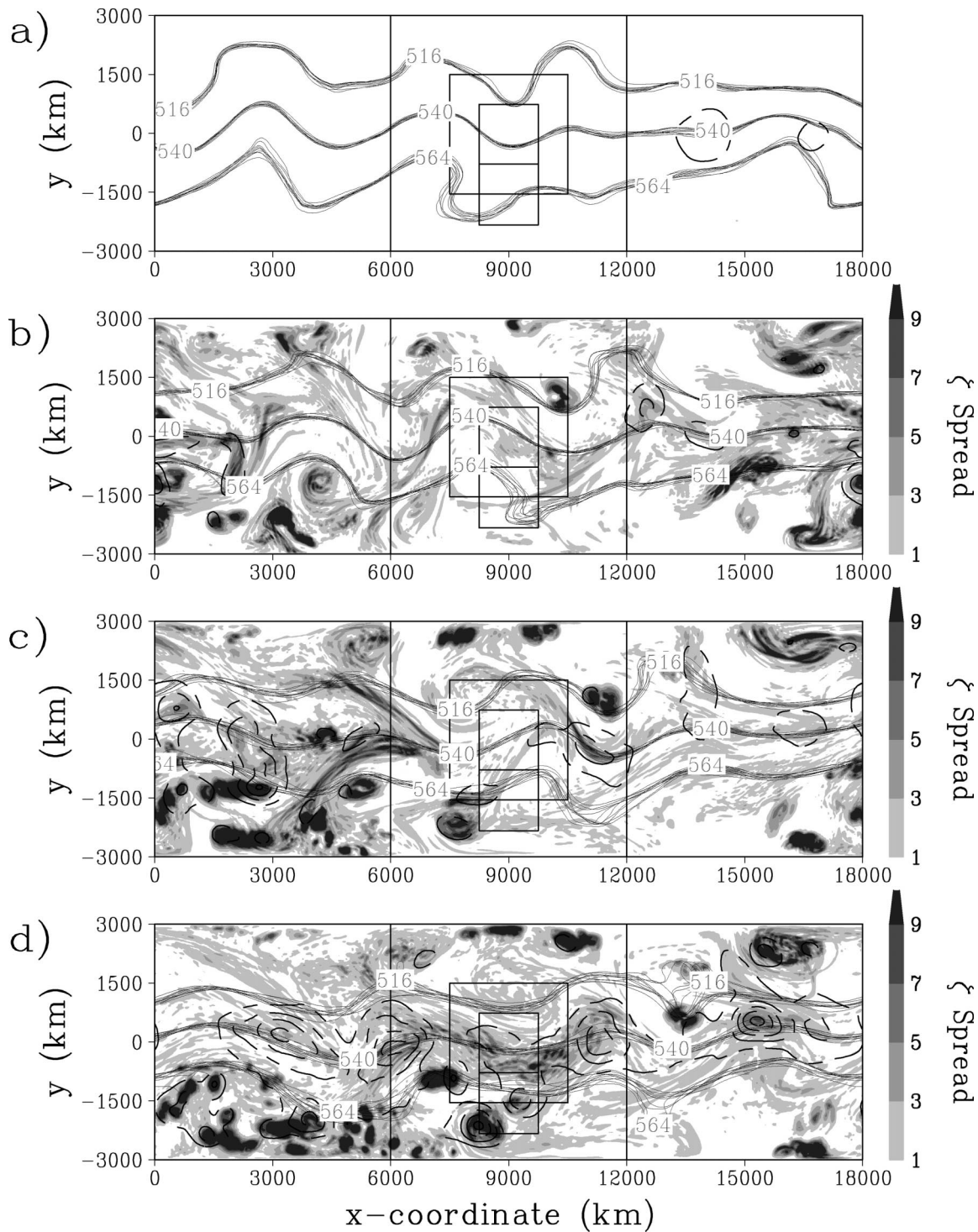


FIG. 2. Example case showing ensemble dispersion [Eq. (14)] for (a) day 0, (b) day 2, (c) day 4, and (d) day 6. A “spaghetti” plot drawn with solid black lines shows the  $(516, 540, 564) \times 10^6 \text{ m}^2 \text{ s}^{-1}$  streamlines from each of the 10 ensemble members. Vorticity dispersion, or spread, is shaded ( $\times 10^{-10} \text{ s}^{-2}$ ), while streamfunction dispersion is shown with dashed contours at  $2 \times 10^{12} \text{ m}^4 \text{ s}^{-2}$  intervals. Nested grid outlines from Fig. 1 are shown for perspective.

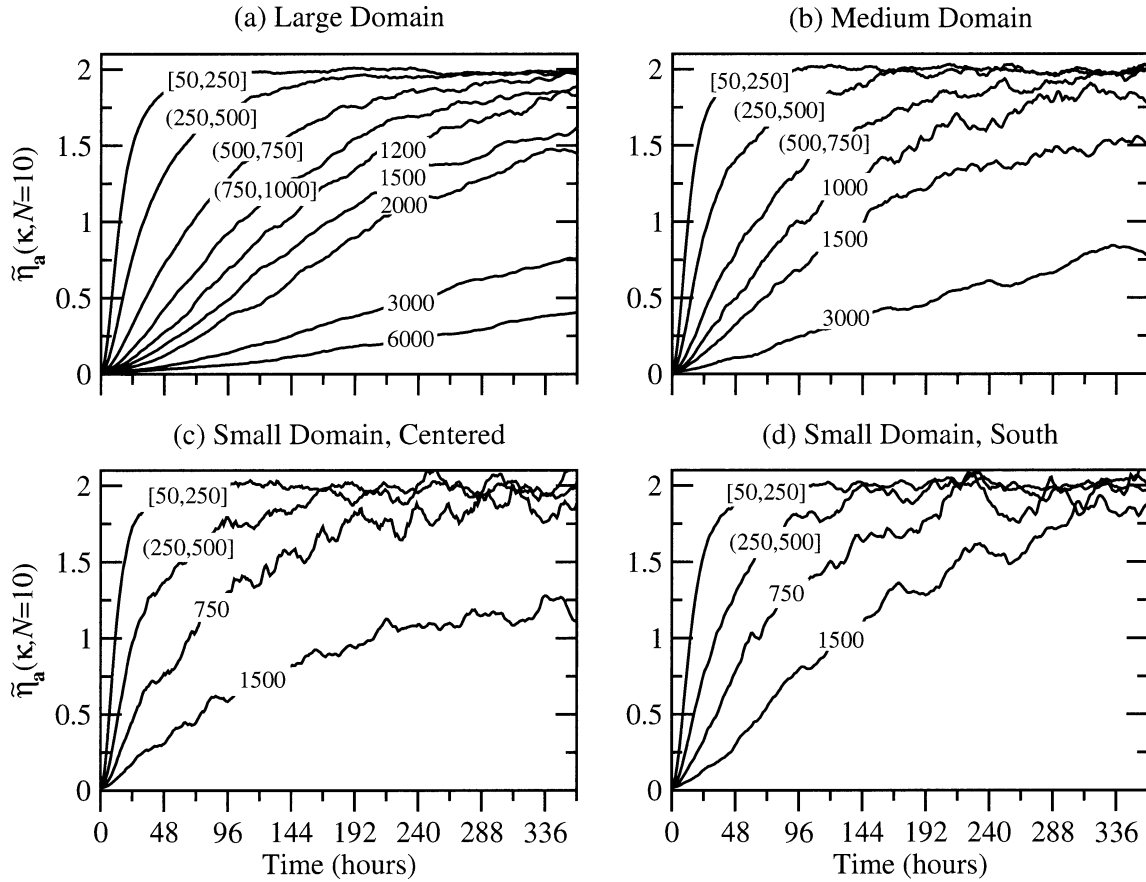


FIG. 3. Normalized vorticity error variance, averaged over 100 independent 10-member global ensemble simulations. Error variances are shown for specific wavelengths (km) or accumulated over 250-km wavelength bands as indicated by the labels on each curve.

placed outside the central shear zone. To see this, note the enhanced spread among the  $516 \times 10^6$  and  $564 \times 10^6 \text{ m}^2 \text{ s}^{-1}$  “spaghetti” streamlines near troughs and ridges in Fig. 2 compared to the central  $540 \times 10^6 \text{ m}^2 \text{ s}^{-1}$  streamlines. The large and medium domains encompass broader regions that include areas outside the central shear zone and therefore have error variance values at 1500-km wavelengths that are between the two extremes seen on the smallest domains.

Several of the curves in Fig. 3 slightly exceed at times the expected maximum value of 2. This result is explained by noting that IC perturbations introduced additional vorticity into the system. Consequently, the vorticity variance of forecasts averaged over all cases is up to 10% greater than the climate vorticity variance of analyses. If error variances are normalized by the variance of perturbed forecasts rather than the variance of unperturbed analyses, all the curves remain less than or equal to the maximum expected value of 2 (not shown). Since the difference is less than 10%, error variances continue to be normalized by analysis variances to remain consistent with the statistical notation as defined in section 2.

### c. Ensemble bias, dispersion, and MSE

Equation (11) was derived to help link error variance spectra to ensemble dispersion. To compare the relative magnitudes of each term in this expression, the following ensemble summary statistics are shown in Fig. 4:

- Ensemble dispersion,  $D^2 = 1/N \sum_{i=1}^N \|\mathbf{f}_i - \bar{\mathbf{f}}\|^2$ ,
- Total biased error variance,  $\sigma^2 = 1/N \sum_{i=1}^N \sum_{\kappa=1}^{K-1} 2|F_i(\kappa)|^2$ ,
- Ensemble mean squared spatial error,  $(\text{sme})^2 = 1/N \sum_{i=1}^N (\langle \mathbf{f}_i \rangle - \langle \mathbf{a} \rangle)^2$ ,
- Grid mean square of the ensemble mean error,  $(\text{eme})^2 = \|\bar{\mathbf{f}} - \mathbf{a}\|^2$ ,
- Ensemble mean square error,  $S^2 = 1/N \sum_{i=1}^N \|\mathbf{f}_i - \mathbf{a}\|^2$ .

The ensemble mean-square error is included to highlight the balance of terms in Eqs. (6) and (10). The results shown in Fig. 4 show that the sum of ensemble mean error “(eme)<sup>2</sup>” and ensemble dispersion  $D^2$  equal the ensemble mse ( $S^2$ ) at all times and on all limited-area domains. This result shows that basic error growth characteristics of the simplified PPV model ensemble behave as expected.

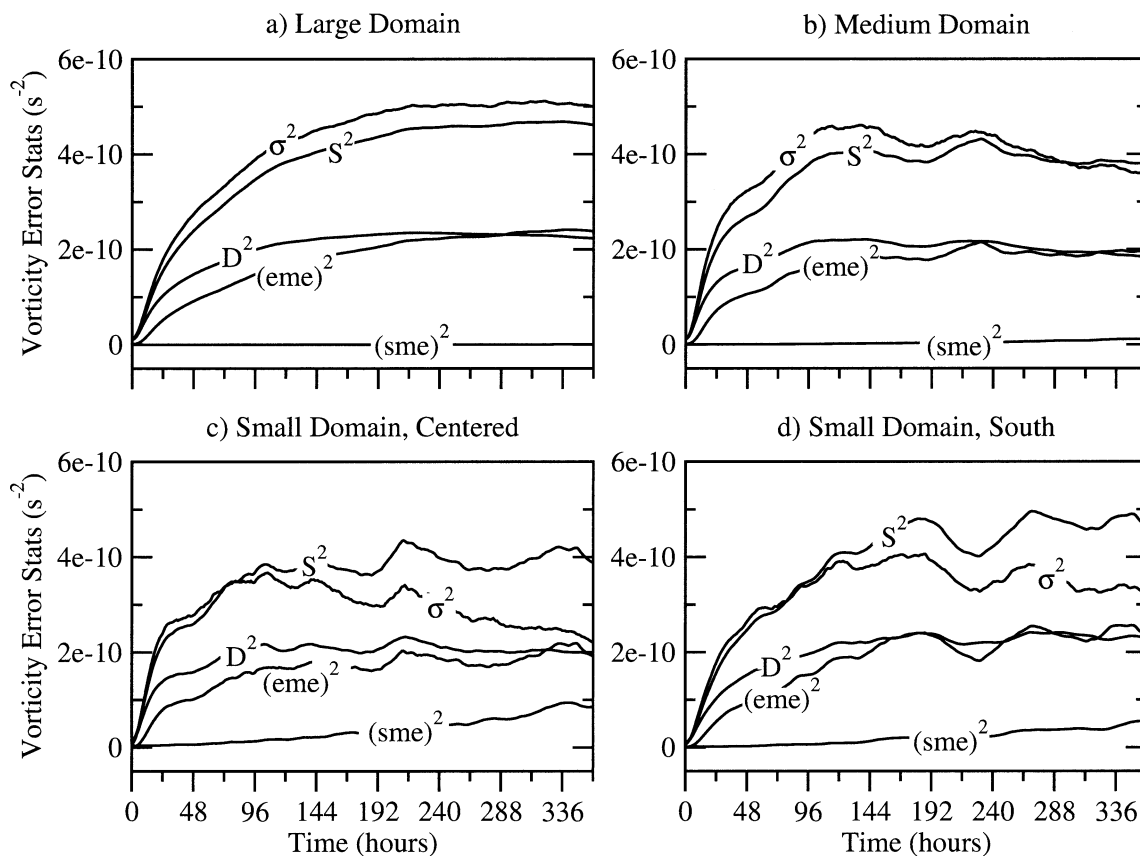


FIG. 4. Ensemble summary statistics for vorticity ( $\times 10^{-10} \text{ s}^{-2}$ ), averaged over 100 independent 10-member global ensembles. See text (section 4c) for a description of variables shown.

On the other hand, Eq. (10) suggests that  $\sigma^2$  is a good approximation for the ensemble MSE, provided that the ensemble average spatial-mean error is small. Since the spatial-mean error term is positive,  $\sigma^2$  must be less than or equal to  $S^2$ . Figures 4a and 4b reveal the contradictory result that  $\sigma^2$  is up to 15% greater than  $S^2$  on the large and medium domains. This contradiction is explained by the fact that removal of linear trends from the data fields prior to calculating Fourier transforms introduces additional variance in higher wavenumbers (Errico 1985). Indeed, the error variance curve obtained from the periodic global domain (not shown)—where detrending is not required—is almost identical to the  $S^2$  curve in Fig. 4a. On both the small domains (Figs. 4c,d), the spatial bias term becomes nontrivial about 5 days into the simulations. At this point, the relationship between  $\sigma^2$  and  $S^2$  predicted by Eq. (10) is confirmed. Specifically, as errors grow toward longer wavelengths exceeding the size of the smaller subdomains ( $1500 \text{ km}^2$ ), the spatial mean error grows larger and contributes to a reduction of  $\sigma^2$  relative to  $S^2$ .

Although we cannot decompose directly the contributions made by various wavelengths to ensemble dispersion, it is possible to decompose the total error var-

iance, which is then related back to ensemble dispersion and ensemble MSE. The only limitation to this argument is the effect of spatial biases. The spatial biases shown in Fig. 4 are small, thus enabling the link between ensemble dispersion and error variance contributions at different wavelengths as defined by Eq. (11).

## 5. Effects of coarsely resolved LBCs

Consider now the impact of applying coarsely resolved LBCs in otherwise perfect simulations. Coarsely resolved LBC fields are generated by applying a low-pass spatial filter to fields from global model simulations running at the same resolution as the LAM. The low-pass filter is a Fourier transform procedure (Errico 1985; Laprise et al. 2000; Nutter 2003) that removes completely all wavelengths shorter than 150 km while perfectly retaining the amplitudes of wavelengths longer than 450 km. The filtering process preserves the accuracy of large-scale motions while removing those which would not be present on a grid having 3 times less spatial resolution as the LAM grid. All simulations in this section are run with hourly updated LBCs by applying linear interpolation in time between updates.

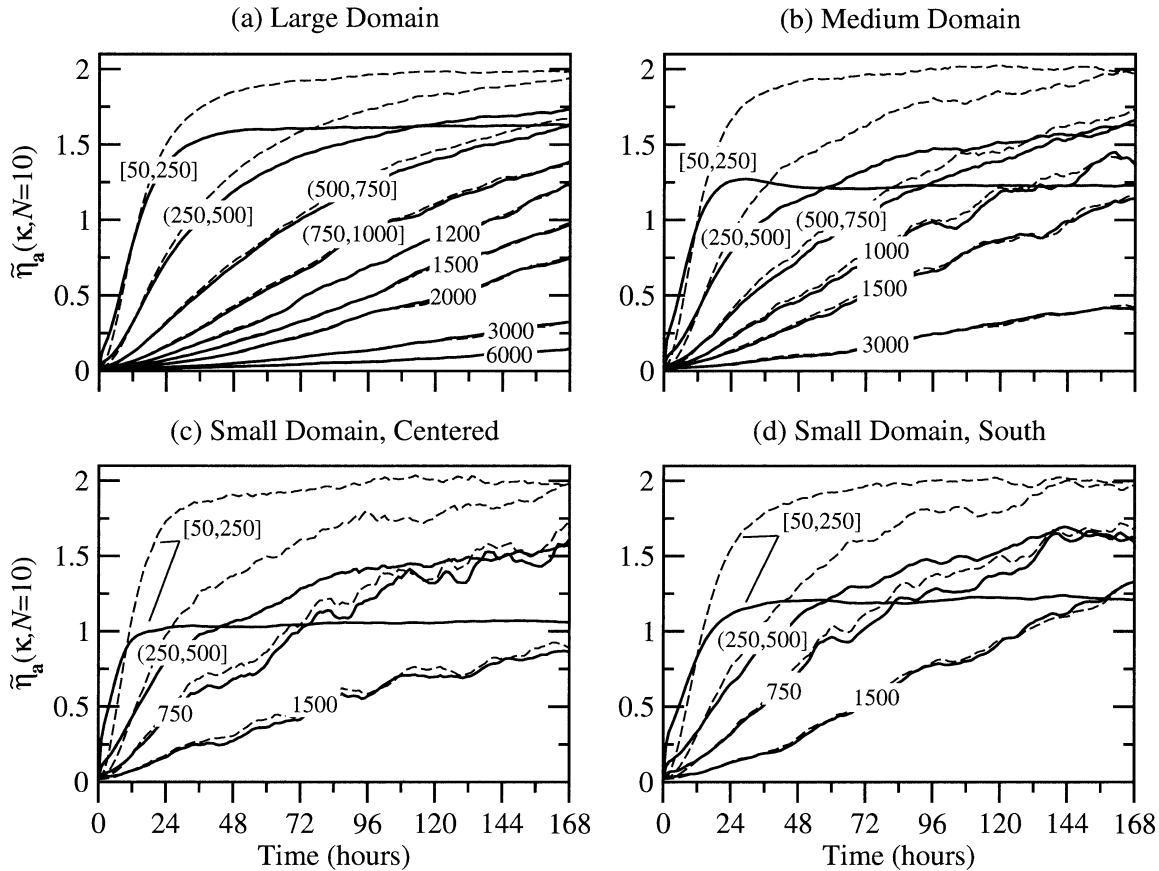


FIG. 5. Normalized vorticity error variance [Eq. (12)], averaged over 100 independent 10-member LAM ensemble simulations having hourly updated, low-pass-filtered LBCs (150-km wavelength cutoff). Line labels (km) indicate wavelengths(s) contributing to error variances. Dashed reference lines are reproduced from Fig. 3, showing error variances from subsets of the global ensemble simulations.

Test runs using LBCs updated every time step revealed only trivial differences from the results presented below. The experimental procedure is similar to that used most recently by Laprise et al. (2000), De Elía and Laprise (2002), and Denis et al. (2002b, 2003). The effect of temporal interpolation between LBC updates is isolated and is described in section 6.

#### a. Ensemble error variance spectra

One hundred independent 10-member LAM ensemble simulations are run using hourly updated, low-pass-filtered LBCs. Initial conditions and LBCs for individual LAM ensemble members are obtained as direct subsets of the corresponding global ensemble members (section 4a), with filtering applied before extracting LBC fields. Error growth in the ensemble occurs due to IC perturbations, use of one-way LBCs, and lack of small scales in filtered LBCs. Comparison of error variance spectra to those from the global ensemble simulations in section 4b provides a direct measure of the impact of using coarsely resolved LBCs.

When simulations are configured with unfiltered (fully resolved) ICs and low-pass-filtered (coarsely re-

solved) LBCs (Fig. 5), error variances in the 50–250-km wavelength band grow rapidly and reach saturation after about 24 to 36 h. The shortwave error variances saturate at values that are about 20% smaller than those from the global ensembles on the large grid and about 40%–50% smaller on the medium and small grids. Furthermore, error variance growth is constrained at larger scales up to about 750 km. It is clear from these results that the absence of small scales in the LBCs places strong constraints on the maximum values of error variance spectra at small scales. This conclusion is consistent with those obtained in several previous studies using more complex models (e.g., Anthes et al. 1985; Anthes 1986; Errico and Baumhefner 1987; Anthes et al. 1989; Vukicevic and Paegle 1989; Vukicevic and Errico 1990; Hamill and Colucci 1997; Paegle et al. 1997; Warner et al. 1997; Du and Tracton 1999; Hou et al. 2001).

An alternative way to view the impact of coarsely resolved LBCs is to divide the LAM variance spectra by the variance spectra obtained on subsets of the global control simulations. This ratio should be unity for perfect LAM simulations. The results in Fig. 6a show the absence of small scales in the filtered initial con-

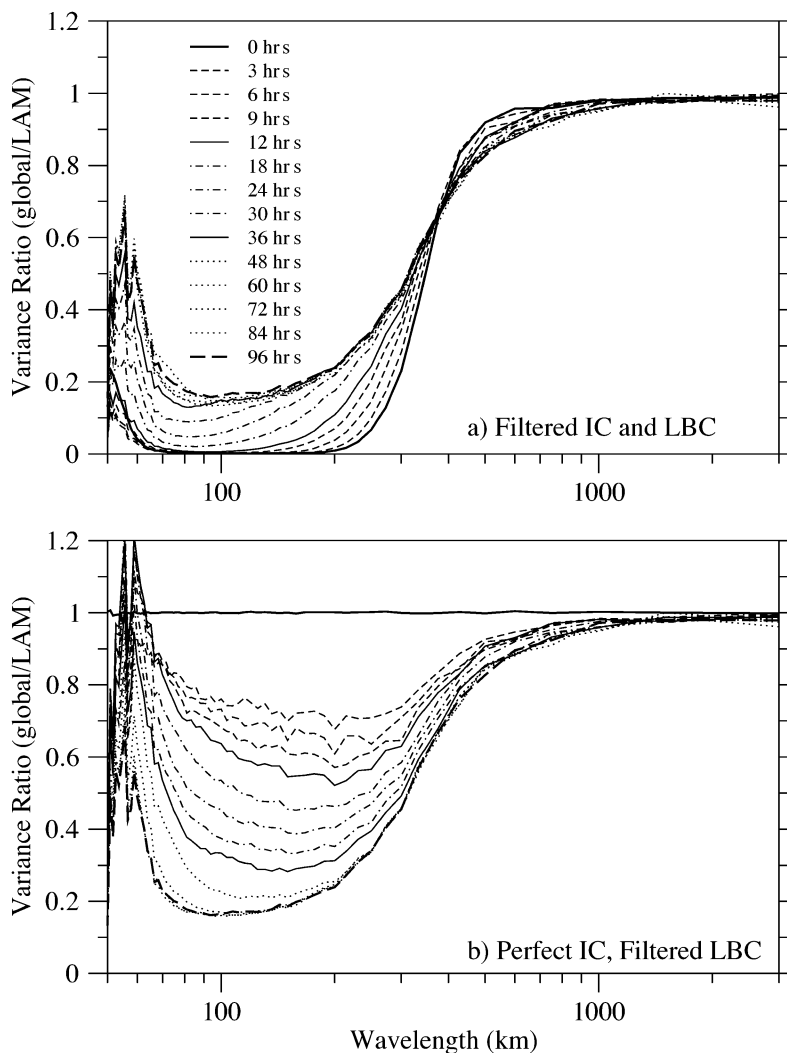


FIG. 6. Ratio between vorticity variance spectra global and LAM simulations on the medium domain shown as a function of time. (a) Simulations are run with low-pass-filtered ICs and hourly updated LBCs (150-km wavelength cutoff). (b) Simulations are run with perfect (unfiltered) ICs and low-pass-filtered LBCs.

ditions. As the simulation progresses, dynamic downscaling produces variance at small scales, but “sweeping” of coarsely resolved LBCs constrains the LAM variance saturation to less than 20% of the variance from the laterally unbounded simulations. In Fig. 6b, small-scale variance declines with time as features pass through the domain and are not reproduced by downscaling effects. Saturation occurs again at just under 20% of the variance for global simulations. The saturation level is dependent on domain size and moves closer to unity on larger domains (not shown) since dynamic downscaling has more time to redevelop smaller-scale features before they are swept through the downstream boundary. The saturation level also depends on model dynamics, since small scales will

develop more quickly in a more unstable model (cf. Fig. 8 in De Elía and Laprise 2002).

#### b. Ensemble summary statistics

The same set of ensemble summary statistics are presented as in section 4c to quantify the impact of error variance constraints on LAM ensemble dispersion. For clarity, the statistics are now shown in Fig. 7 as differences between those calculated from the global and the LAM ensembles.

The loss of error variance at small scales noted in Fig. 5 appears as a decrease in total error variance in the LAM ensembles compared to that of the global ensembles on all domains after about 12 h. The LAM

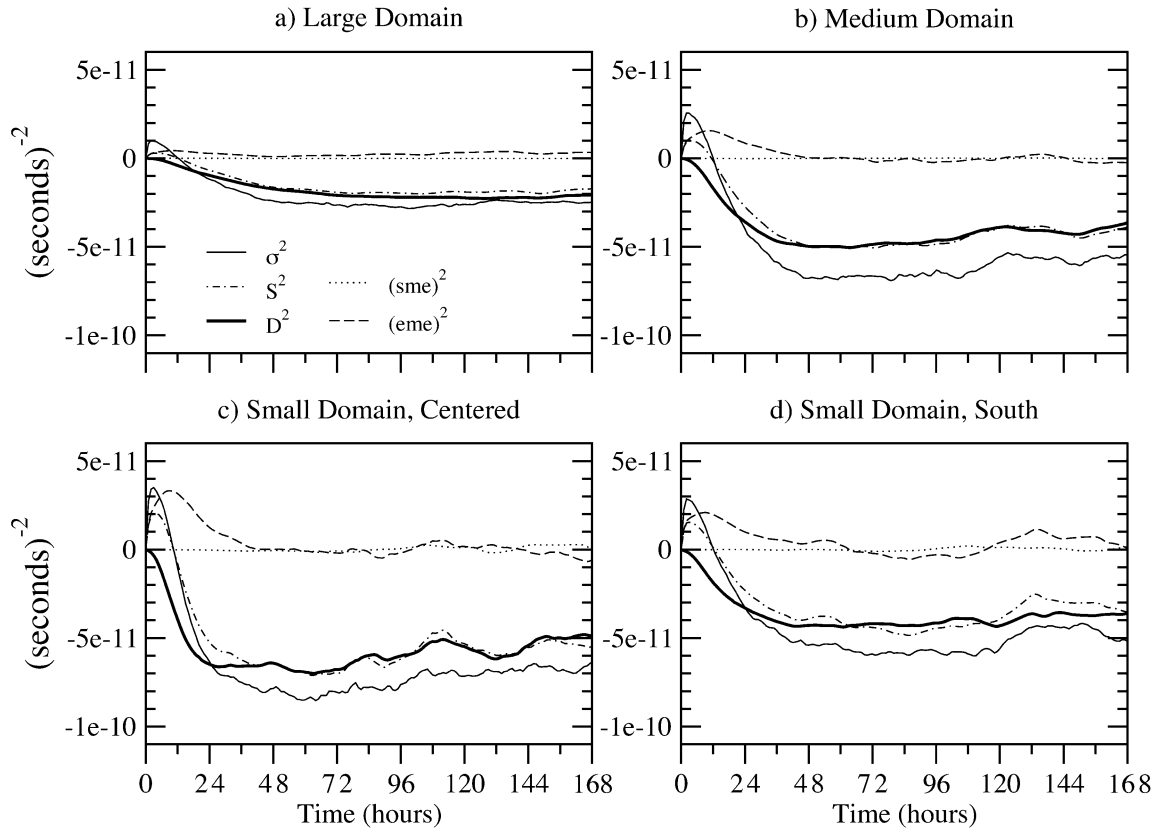


FIG. 7. Difference in vorticity summary statistics (section 4c) for LAM ensemble simulations having hourly updated, low-pass-filtered LBCs (150-km wavelength cutoff) compared to statistics from global ensemble simulations as shown in Fig. 4. Results are averaged over 100 independent 10-member ensemble simulations. On ordinate, “e” denotes base-10 exponential notation.

ensemble dispersion also is less than that of the global ensembles on all domains. Since the bias terms remain nearly unchanged, the loss of dispersion is attributed directly to the loss of error variance at small scales [Eq. (11)]. The loss of dispersion is most notable on the medium and small domains, where it is reduced by about 10% to 40%. The magnitude of decrease is related to the size of domain and advective time scale of features passing through the domain (Warner et al. 1997).

An interesting characteristic noted on all domains is the increase in total error variance in the LAM simulations during the first 12 h. Close examination of Fig. 5 shows that this increase in variance is contributed at smaller scales. The source of this extra variance early in the LAM simulations is due to the different solution obtained by solving the Helmholtz equation to obtain streamfunction from smoothed LBCs. This introduces the error variance at small scales and also contributes to an increase in ensemble mean error (Fig. 7). As small-scale features are swept from the LAM domain, error variance becomes negative relative to the global simulations because error growth is constrained. In spite of the initial increase in error variance, ensemble dispersion remains decreased in all simulations because of the

increase in ensemble mean error in the absence of changes in the spatial bias [see Eq. (11)].

## 6. Effects of temporally interpolated LBCs

### a. LBC error “pulsing”

Using a highly controlled model configuration, it was demonstrated above that the “sweeping out” of small-scale features by coarsely resolved LBCs is sufficient to limit ensemble dispersion by constraining error variance growth. We now present an example simulation to highlight the similar, and often neglected, error growth behavior introduced by temporal interpolation between available LBC updates. The example case shown in Fig. 8 is perfect except for errors created using 3-hourly interpolated LBCs. The initial and lateral boundary conditions are subsets of output from a full-channel simulation running at the same resolution as the LAM model. The IC is not shown because it has no error.

During the first 1.5 h of the simulation (Figs. 8a–c), errors develop within the peripheral seven-point wave-absorbing zone because of differences between the linearly interpolated LBC and the interior solution. Then,

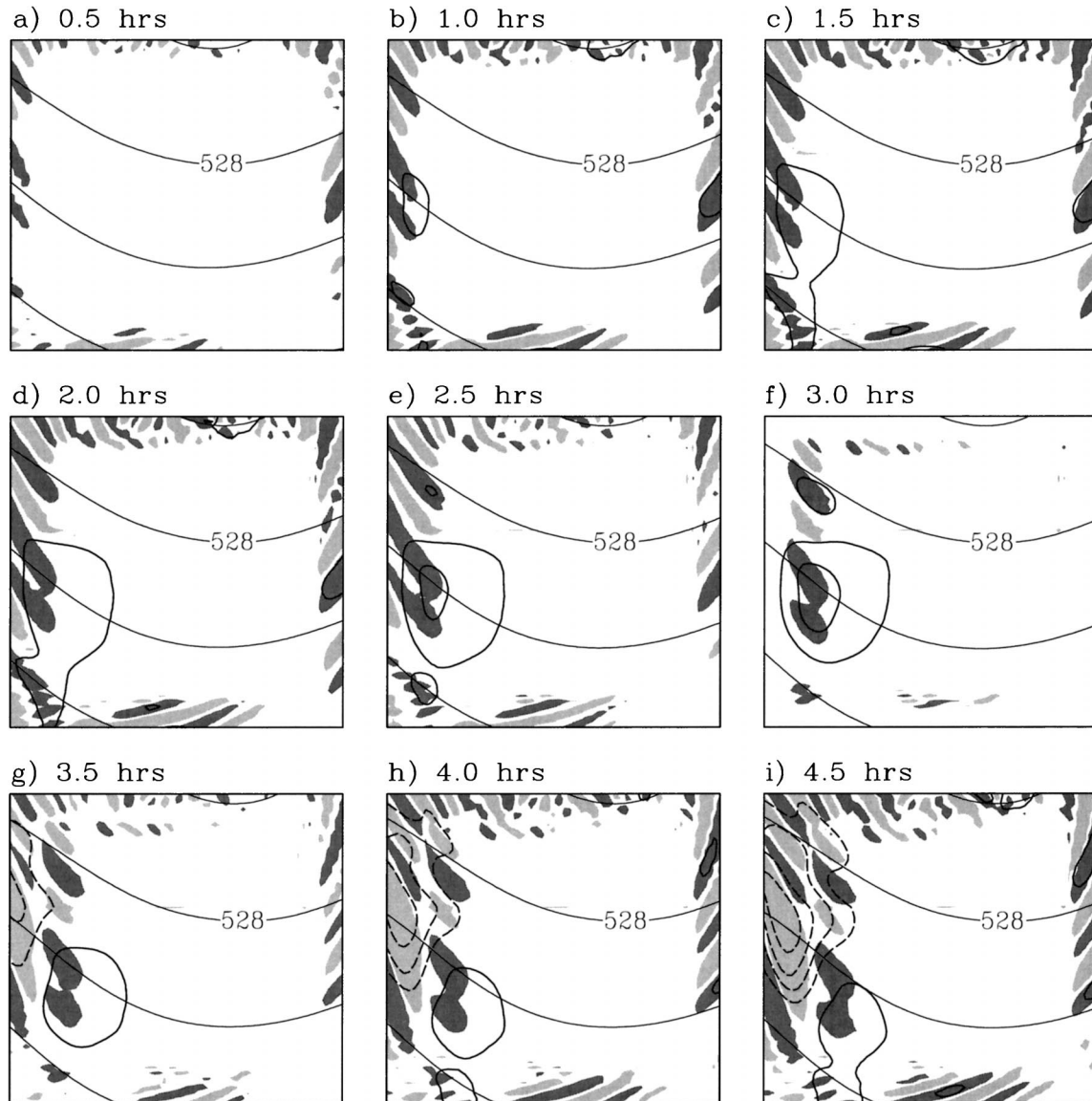


FIG. 8. Example LAM simulation run on the small, center domain (Fig. 1) showing effects of LBC update interval in an otherwise perfect simulation. LBCs are given every 3 h and are linearly interpolated at each step between the updates. Gentle curves are streamlines from the control simulation that provides the LBCs ( $12 \times 10^6 \text{ m}^2 \text{ s}^{-1}$  intervals). Positive (negative) vorticity errors exceeding  $0.5 \times 10^{-5} \text{ s}^{-1}$  are indicated by light (dark) shades. Positive (negative) streamfunction errors are shown with solid (dashed) contours at  $\pm 5 \times 10^4 \text{ m}^2 \text{ s}^{-1}$  intervals (zero line omitted).

from 2 to 3 h (Figs. 8d–f), errors within the buffer zone decline and vanish. This error growth “pulse” repeats between subsequent 3-hourly updates of perfect LBCs, with the peripheral errors vanishing at 3, 6, and 9 h (Figs. 8f, 8l, and 8r). Errors in the buffer zone are greatest near the midpoint of the LBC update cycle when the respective linearly and nonlinearly evolving external and internal solutions are most inconsistent. Once introduced, the LBC pulse errors continue to propagate inward and modify the LAM solution. As the LAM solution becomes more infected with each successive error “pulse,” the LBC inconsistency becomes stronger

and generates larger errors, which then propagate farther inward.

The example simulation demonstrates that the LBC update interval determines the spatial scale of errors that can be introduced by aliasing of fields passing through the lateral boundary, provided that advection or wave propagation is the main cause of local changes in the solution. To formalize this argument, suppose a wave passes through the boundary with speed  $|c_x|$ . If the LBC is updated with frequency  $f_{\text{LBC}}$ , then the minimum wavelength that can be fully sampled is  $\lambda_{\text{LBC}} = 2|c_x|/f_{\text{LBC}}$ . Thus, the minimum spatial scale of aliasing

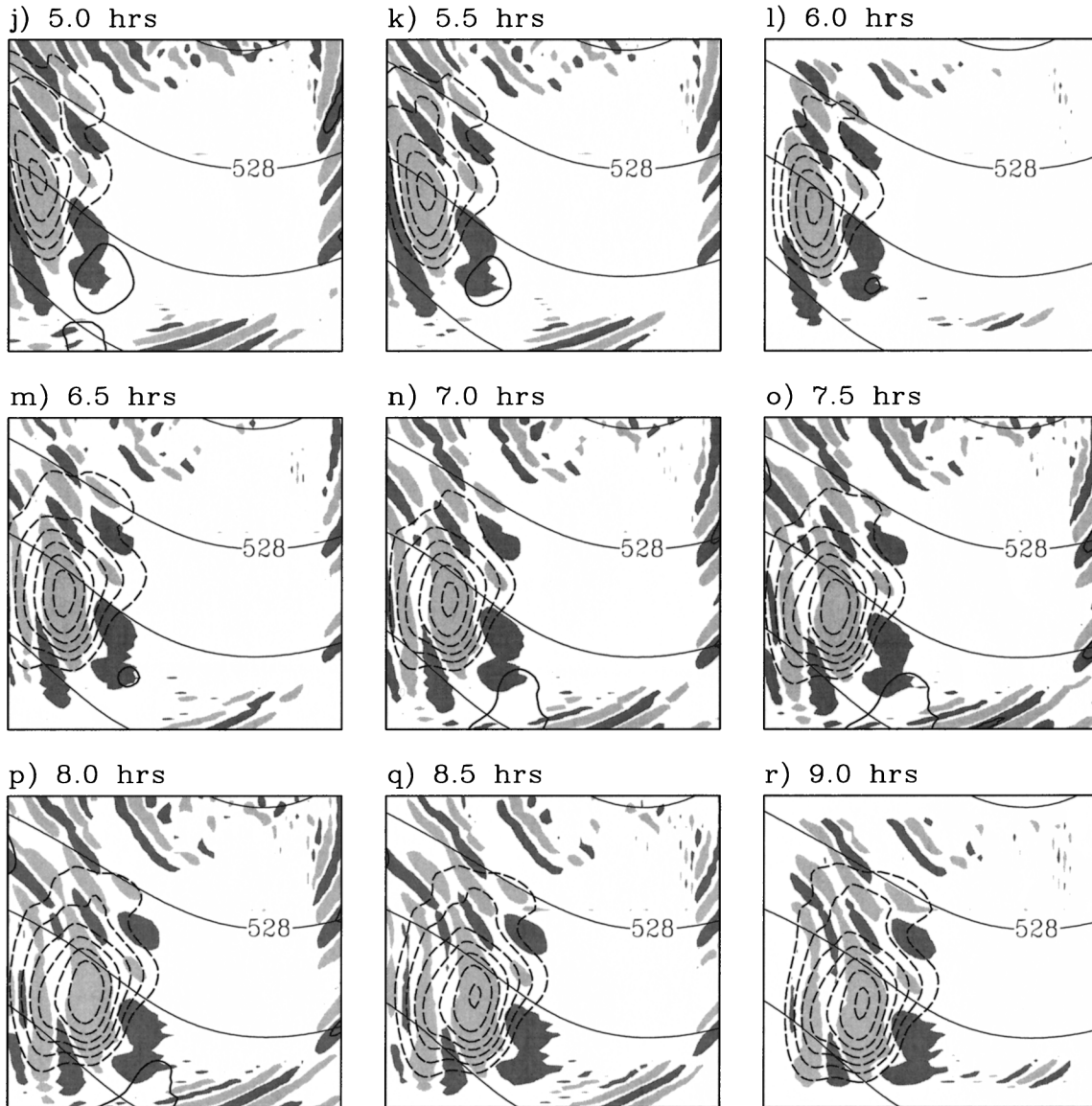


FIG. 8. (Continued)

errors introduced while waves pass through the boundary increases with less frequent LBC updates. If this minimum scale is longer than the smallest resolved wavelength on the LAM domain, then LBC pulsing errors will contribute to constraints on error variance growth while “sweeping” through the domain. LBC pulsing errors are maximized at small scales due to the filtering effect, but may also form at larger scales by slightly reducing the amplitude of all nonstationary waves passing through the lateral boundary.

The Rossby wave phase relation can help quantify the temporal filtering effect for the PPV model used in this study. Zonal phase speeds for waves passing through the boundary are given by  $c_x = U_0 - \beta/(k^2 + l^2)$ . Assuming zonal flow ( $l = 0$ ),  $k = 2\pi/L_x$ , and  $|c_x|$  defined above, we find that  $\lambda_{\text{LBC}} = 2|U_0 - \beta L_x^2/4\pi^2|/f_{\text{LBC}}$ . Results ob-

tained from this expression for selected nesting frequencies and appropriate choices for constants  $U_0$  and  $\beta$  are shown in Fig. 9. There is a cusp in the curves for external wavelengths of  $\sim 5400$  km where the Rossby waves are stationary and do not suffer any filtering due to temporal interpolation of LBCs. All values of  $\lambda_{\text{LBC}}$  are positive because the absolute value of  $c_x$  was used.

The results in Fig. 9 show that for half-hourly updated LBCs, all waves are sampled well enough to have adequate spatial resolution on the LAM domain. When using hourly updated LBCs, external wavelengths less than 3000 km move fast enough to produce aliasing errors at scales up to about 100 km. Since less than 1% of the total vorticity variance in this model is represented by these scales (Nutter 2003), LBC pulsing errors remain negligible if LBCs are updated at least once per

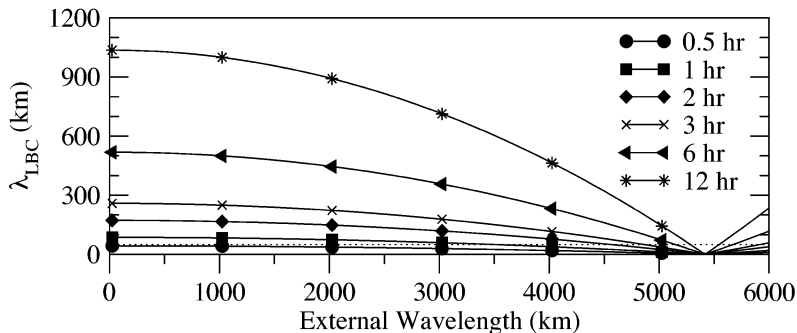


FIG. 9. Minimum resolved spatial scale of aliasing error after temporal filtering due to linear interpolation of LBCs between available updates at indicated intervals. The dotted horizontal line marks the smallest  $2\Delta x = 50$  km wavelength resolved on the LAM domain. See text for additional description.

hour. When using 3-hourly LBC updates, external wavelengths shorter than 3000 km generate aliasing errors at scales no smaller than 150 km while passing through the lateral boundary.

The vorticity errors in the example case (Fig. 8) produce approximately 5 to 10 anomaly couplets along each side of the domain. Since each side has a length of 1500 km, this result suggests that the vorticity errors in this example from at wavelengths of about 150 to 300 km. This estimate is similar to those indicated in Fig. 9 for 3-hourly LBC updates.

The LBC pulse error is seen on each of the four domains tested (not shown in examples), but takes longer to propagate across the medium (3000 km)<sup>2</sup> and large (6000 km)<sup>2</sup> domains. As expected, the pulse effect is less pronounced when using hourly LBC updates and more pronounced when using 6-hourly LBC updates. Note that in practical applications the LBC pulse effect could be swamped by other errors when the LBCs are given by discordant external analyses or forecasts. Furthermore, note that the distribution of phase speeds varies with the complexity of the synoptic setting. Therefore, the intensity at which LBC pulse errors are produced also varies with time and location.

#### b. Ensemble error variance spectra

Consider next the the impact of temporal interpolation of LBCs on error growth in LAM ensemble simulations using the same statistical framework as above. Statistics are averaged over 100 independent 10-member ensemble simulations. Initial conditions and LBCs for individual LAM ensemble members are again obtained as direct subsets of the corresponding global ensemble members (section 4a). Since LBCs are fully resolved (unfiltered), the only sources of error growth are IC perturbations and the use of temporally interpolated one-way LBCs. The impact of LBCs on the LAM ensemble simulations is determined as before by comparing error variance spectra directly to those obtained from the laterally unbounded global simulations.

Experiments were run using LBCs updated at hourly, 3-hourly, and 6-hourly intervals. Given hourly LBC updates, statistical results (not shown) revealed that error variance growth was not seriously degraded because the LBCs were sampled with adequate frequency to avoid the filtering effect described earlier (Nutter 2003). The results presented here are obtained from simulations having 3-hourly updated LBCs. Results from simulations having 6-hourly updated LBCs (not shown) reinforce the concept that LBC constraints on error variance growth increase with longer LBC update intervals (Nutter 2003).

Given 3-hourly LBC updates (Fig. 10), losses of error variance occur at small scales due to ongoing LBC sweeping of filtered inflow caused by inadequate temporal sampling. Saturation values in the shortest wavelength band range from about 1.5 on the small-centered grid to about 1.75 on the large domain. Thus, the filtering response from 3-hourly LBC interpolation reduces maximum shortwave error variance growth by about 10% to 25% from the expected value of 2. Smaller reductions are seen in spatial scales up to around 750 km. The LBC error pulse is also evident, although the magnitude of oscillations accounts for at most about 5% of the error variance values in the 50–250-km wavelength band at saturation. Hence, IC perturbations are the dominant source of error growth for these ensemble simulations. Comparison of these results to those in Fig. 5 reveals that the use of coarsely resolved LBCs provides a stronger constraint on error growth than does temporal interpolation between LBC updates.

#### c. Ensemble summary statistics

Using the same format as in section 5b, Fig. 11 shows how the loss of error variance at small scales due to interpolation between 3-hourly LBC updates affects overall ensemble behavior. The total error variance ( $\sigma^2$ ) decreases on all domains relative to the global simulations after about 12 to 24 h due to the LBC filtering effect discussed earlier in section 6a. The error pulse

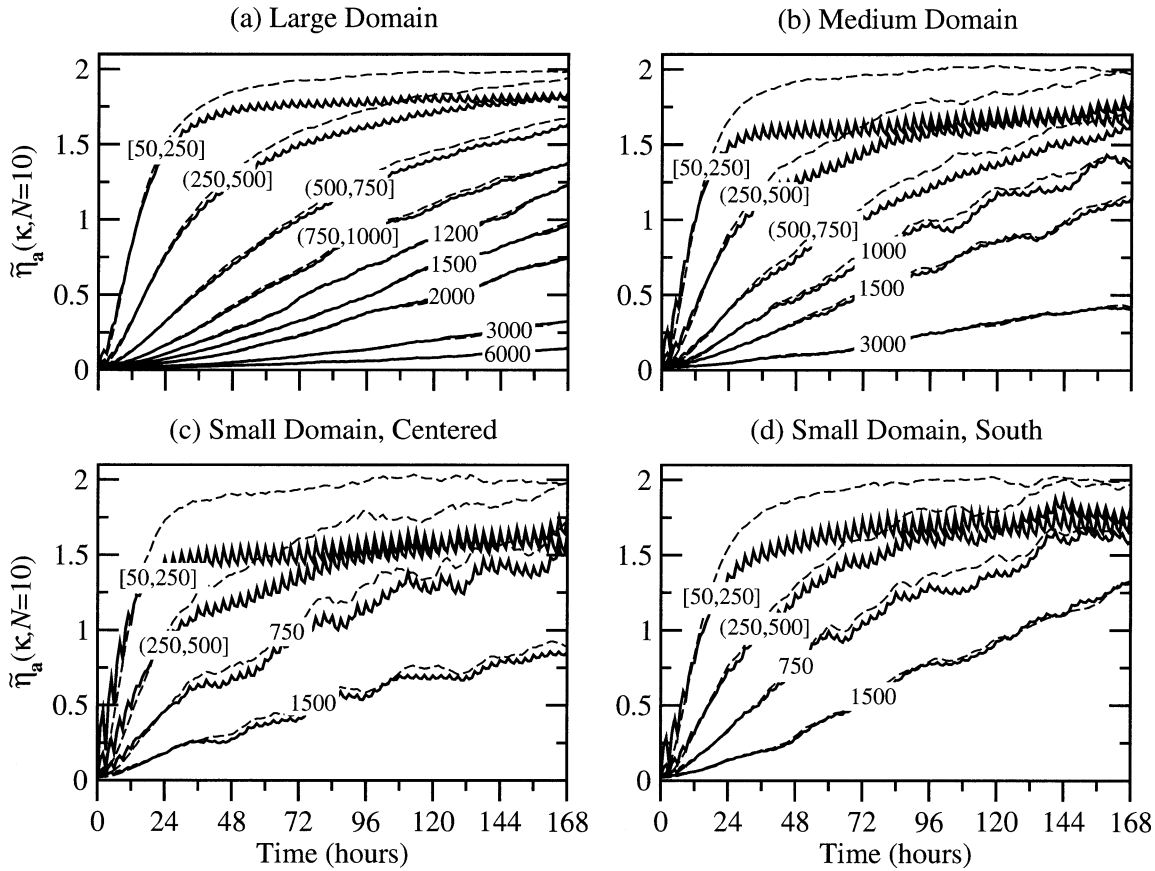


FIG. 10. As in Fig. 5, except for LAM ensemble simulations having 3-hourly updated, unfiltered (fully resolved) LBCs.

associated with perfect 3-hourly LBC updates also appears as discussed in section 6a. The spatial bias remains nearly identical for both LAM and global ensembles. Thus, following Eq. (11), the increases in both  $\sigma^2$  and ensemble mean error (eme<sup>2</sup>) during the first 24 to 48 h offset each other so that the LAM ensemble experiences an immediate loss of dispersion that deepens with time. The initial increases in total error variance and ensemble mean error were explained at the end of section 5b. The LBC error pulse seen in  $\sigma^2$  also affects ensemble dispersion, although the magnitude of the oscillation is small compared to the overall loss of dispersion.

### 7. Example of LAM ensemble dispersion

An example of global ensemble dispersion was shown for one example case in Fig. 2. That same case is run again, but now as a LAM ensemble configured with 3-hourly updated and low-pass-filtered LBCs run on the medium domain (see Fig. 1). As in all previous LAM ensembles, the ICs and LBCs for individual members are obtained as direct subsets of the corresponding global ensemble members.

To visualize the documented loss of ensemble dispersion due to LBC filtering effects, the following loss ratio is defined at each grid point  $p$  in the domain:

$$1 - \frac{\mathbf{d}_p^2(\text{global})}{\mathbf{d}_p^2(\text{LAM})}, \quad (15)$$

where  $\mathbf{d}_p^2$  is the local dispersion defined by Eq. (14). If this loss ratio is negative, then the LAM ensemble has less dispersion than the global ensemble.

The example LAM ensemble and its dispersion loss ratio is shown in Fig. 12. The “spaghetti” contours and streamfunction dispersion appear much the same as in the appropriate portion of the global ensemble (Fig. 2). At the initial time (Fig. 12a), regions of increased and decreased vorticity dispersion relative to the global ensemble appear evenly distributed and similar in magnitude since the loss ratio is near zero everywhere. After 12 h have elapsed (Fig. 12b), regions showing strong reductions of dispersion appear along the upstream side of the domain. At the same time, the dispersion loss ratio remains evenly distributed and near zero within the downstream portion of the domain. The reductions near the upstream boundary are obviously attributed to the spatial and temporal filtering effects associated with the LBCs. The area impacted by loss of dispersion grows with time as LBC errors sweep through the domain from west to east. Locally, the LAM ensemble dispersion loss ratio shows reductions of a factor of 8 or larger. When averaged across the domain, the reduction of LAM en-

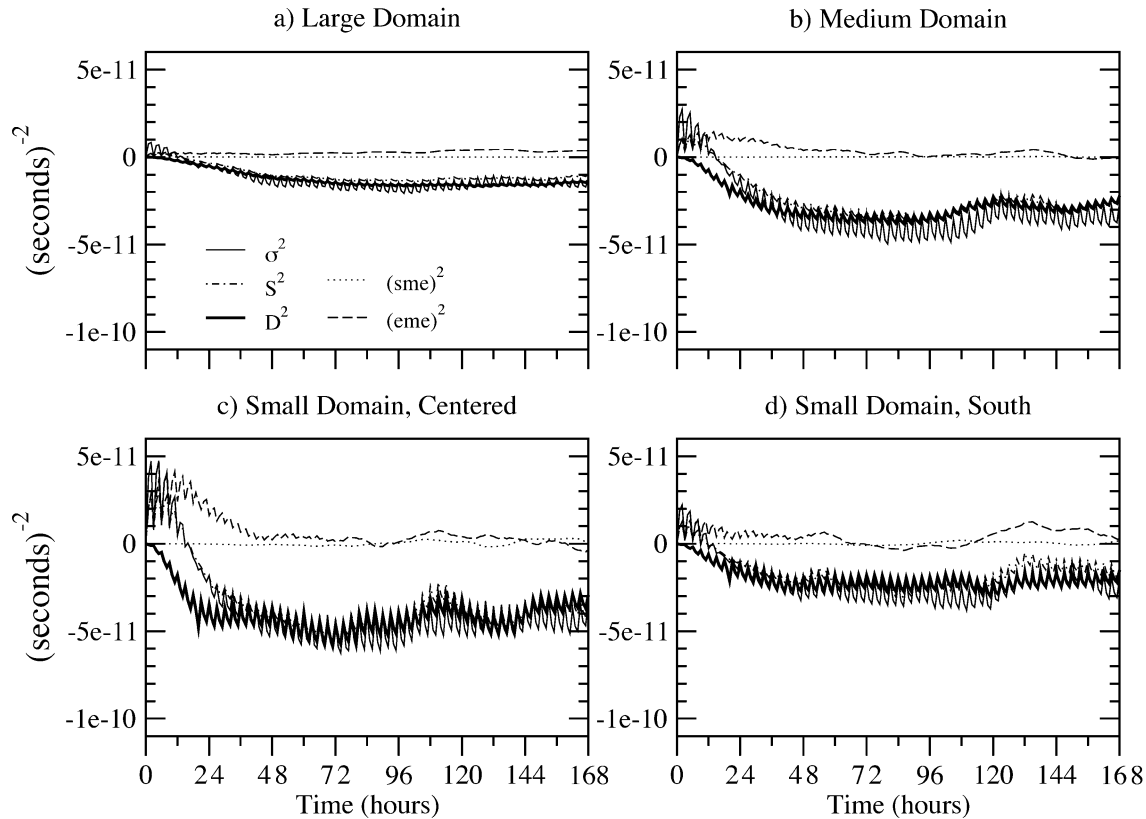


FIG. 11. As in Fig. 7, except for LAM ensemble simulations having 3-hourly updated, unfiltered (fully resolved) LBCs.

semble dispersion shown by this example is consistent with the ensemble summary statistics shown earlier (e.g., Fig. 7).

## 8. Conclusions

LAM ensemble simulations were conducted using a simplified model configuration specifically designed to isolate the impact of infrequently updated or coarsely resolved LBCs on ensemble dispersion. An expression was developed that provides a relationship between ensemble dispersion, error variance spectra, ensemble mean error, and spatial bias. The advantage of analyzing results using error variance spectra is that we can determine which wavelengths are most directly impacted by LBC constraints and measure their collective impact on the loss of LAM ensemble dispersion. It was shown that the ensemble mean error and spatial biases in the LAM ensemble simulations are nearly the same as those from the global ensemble simulations. Therefore, a loss of error variance identified at small scales is sufficient to explain the reduction in LAM ensemble dispersion when using “one-way” LBCs. The loss of dispersion is greater on smaller domains because features are advected more quickly from one side to the other. Hence, LAM ensembles configured with very large domains (such as the NCEP Short-Range Ensemble Forecast sys-

tem) will experience minimal LBC constraints on dispersion, while those configured with smaller domains may experience rather serious constraints.

It is demonstrated that the impact of coarsely resolved LBCs or temporal interpolation of LBCs on error growth in LAM simulations is quite similar. Both act to remove small-scale features from the external fields passing through the lateral boundary, thereby constraining ensemble dispersion. Of the two effects considered here, the impact of coarsely resolved LBCs has a stronger impact than temporal interpolation when the LBC update frequency is reasonably high. The simplified model approach used here removes other factors from consideration that could increase ensemble mean error and ensemble bias, therefore distorting the direct relationship between error variance and ensemble dispersion. Nonetheless, the error growth behaviors shown here are certainly present to some extent in more sophisticated atmospheric models using one-way LBCs and may also exist in global variable resolution models where advection of scale-deficient flow into the high-resolution region will constrain error growth rates at small scales.

An unresolved question from this work is how large is the impact relative to other modeling and LBC data deficiencies. In particular, large-scale LBC errors present in most forecast and analysis systems result from the use of discordant external and nested models. Errors

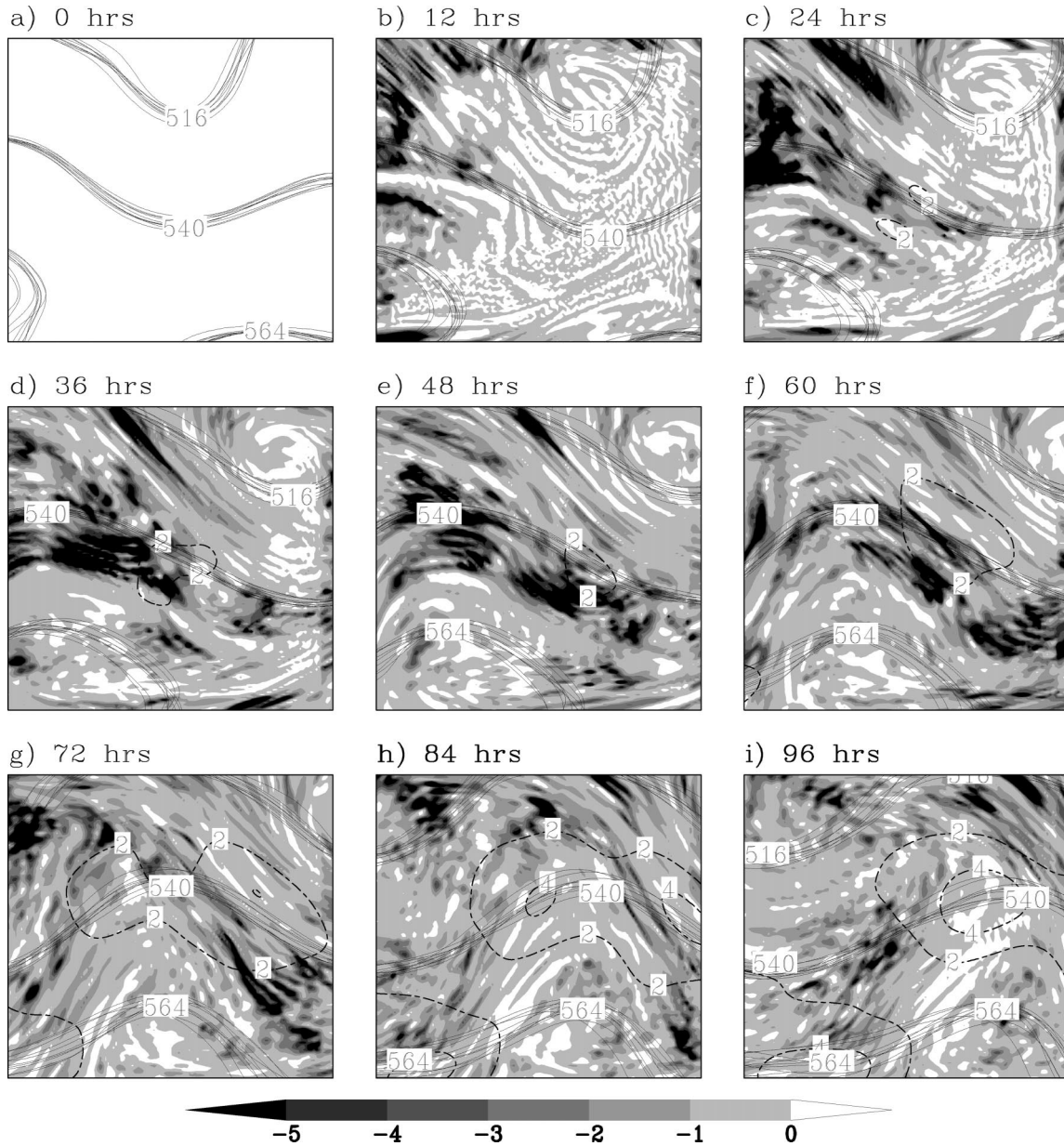


FIG. 12. As in Fig. 2, except shading is the vorticity dispersion loss ratio [Eq. (15)] from an example LAM ensemble run on the medium domain (Fig. 1) having 3-hourly updated, low-pass-filtered LBCs.

of this type are, by design, excluded from the simple model configuration since they are not *caused* by the use of one-way LBCs. It is beyond the scope of the present study to compare the magnitudes of externally created LBC errors versus those specifically created by the use of one-way LBCs.

The results shown here in Figs. 5 and 10 are consistent with those obtained in previous studies using full primitive equation LAMs (Baumhefner and Perkey 1982; Anthes et al. 1985; Errico and Baumhefner 1987; Vukicevic and Paegle 1989; Vukicevic and Errico 1990; Laprise et al. 2000; De Elía and Laprise 2002).

Therefore, error growth behaviors established for other aspects of this work should generalize at least qualitatively to more complex model systems. When considering an extension of the current study to other modeling systems, the magnitude of the LBC constraint will depend on the speed at which waves pass through the lateral boundaries and on the amplitudes of IC perturbations. Furthermore, the time scale needed to reach saturation is likely to decrease, but the shape of the normalized error growth curves should remain unchanged.

Results from this paper suggest the need to apply

finer-scale LBC perturbations at every time of the LAM simulations, especially on LAM domains that are small compared to the advective time scale. The model and analysis method tools developed in the current study form a basis for developing a new method (Nutter 2003) that is designed to help restore the error variance and ensemble dispersion lost through LBC constraints. The new method was developed to apply statistically consistent LBC perturbations that remain spatially and temporally coherent while passing through the boundaries. With a few noted exceptions, the LBC perturbations are shown to capably restore error variance growth and LAM ensemble dispersion without compromising the integrity of the individual solutions. This is the subject of Nutter et al. (2004).

*Acknowledgments.* This research was supported by funding from several sources: the University of Oklahoma (OU) School of Meteorology through the Robert E. Lowry endowed chair; the U.S. Department of Defense under Grant N00014-96-1-1112, or Coastal Meteorology Research Program (CMRP); the Williams Energy Marketing and Trading Company through a Williams Graduate Research Fellowship within the OU Center for Analysis and Prediction of Storms (CAPS); the National Science Foundation under Grant ATM-0129892, related to the International H<sub>2</sub>O Project (IHOP); and the OU Alumni Association Fellowship Program.

The National Severe Storms Laboratory (NSSL) shared desk space and access to a multiprocessor computer. The OU School of Meteorology provided excellent infrastructure and administrative support. Most of the computations were performed on the IBM Regatta p690 symmetric multiprocessor computer operated by the OU Supercomputing Center for Education and Research (OSCER).

Professor René Laprise and a second anonymous reviewer provided constructive comments that helped improve the manuscript.

#### REFERENCES

- Anthes, R. A., 1986: The general question of predictability. *Mesoscale Meteorology and Forecasting*, Amer. Meteor. Soc., 636–656.
- , Y.-H. Kuo, D. P. Baumhefner, R. M. Errico, and T. W. Bettge, 1985: Predictability of mesoscale atmospheric motions. *Advances in Geophysics*, Vol. 28, Academic Press, 159–202.
- , —, E.-Y. Hsie, S. Low-Nam, and T. W. Bettge, 1989: Estimation of skill and uncertainty in regional numerical models. *Quart. J. Roy. Meteor. Soc.*, **115**, 763–806.
- Arakawa, A., 1966: Computational design for long-term numerical integrations of the equations of fluid motion: Two-dimensional incompressible flow. Part i. *J. Comput. Phys.*, **1**, 119–143.
- Baumhefner, D. P., 1984: The relationship between present large-scale forecast skill and new estimates of predictability error growth. *Predictability of Fluid Motions*, G. Holloway and B. J. West, Eds., American Institute of Physics, 169–180.
- , and D. J. Perkey, 1982: Evaluation of lateral boundary errors in a limited-domain model. *Tellus*, **34**, 409–428.
- Boer, G. J., 1984: A spectral analysis of predictability and error in an operational forecast system. *Mon. Wea. Rev.*, **112**, 1183–1197.
- Charney, J. G., R. G. Fleagle, V. E. Lally, H. Riehl, and D. Q. Wark, 1966: The feasibility of a global observation and analysis experiment. *Bull. Amer. Meteor. Soc.*, **47**, 200–220.
- Dalcher, A., and E. Kalnay, 1987: Error growth and predictability in operational ECMWF forecasts. *Tellus*, **39A**, 474–491.
- Davies, H. C., 1976: A lateral boundary formulation for multilevel prediction models. *Quart. J. Roy. Meteor. Soc.*, **102**, 405–418.
- , 1983: Limitations of some common lateral boundary schemes used in regional NWP models. *Mon. Wea. Rev.*, **111**, 1002–1012.
- De Elía, R., and R. Laprise, 2002: Forecasting skill limits of nested, limited-area models: A perfect-model approach. *Mon. Wea. Rev.*, **130**, 2006–2023.
- Denis, B., J. Côté, and R. Laprise, 2002a: Spectral decomposition of two-dimensional atmospheric fields on limited-area domains using the discrete cosine transform (DCT). *Mon. Wea. Rev.*, **130**, 1812–1829.
- , R. Laprise, D. Caya, and J. Côté, 2002b: Downscaling ability of one-way nested regional climate models: The big-brother experiment. *Climate Dyn.*, **18**, 627–646.
- , —, and —, 2003: Sensitivity of a regional climate model to the resolution of the lateral boundary conditions. *Climate Dyn.*, **20**, 107–126.
- Du, J., and M. S. Tracton, 1999: Impact of lateral boundary conditions on regional-model ensemble prediction. *Research Activities in Atmospheric and Oceanic Modeling*, H. Ritchie, Ed., WMO TD-942, Rep. 28, 6.7–6.8.
- Durrant, D., 1999: *Numerical Methods for Wave Equations in Geophysical Fluid Dynamics*. Springer-Verlag, 465 pp.
- Errico, R. M., 1985: Spectra computed from a limited area grid. *Mon. Wea. Rev.*, **113**, 1554–1562.
- , 1987: A comparison between two limited-area spectral analysis schemes. *Mon. Wea. Rev.*, **115**, 2856–2861.
- , and D. Baumhefner, 1987: Predictability experiments using a high-resolution limited-area model. *Mon. Wea. Rev.*, **115**, 488–504.
- Hamill, T. M., 2001: Interpretation of rank histograms for verifying ensemble forecasts. *Mon. Wea. Rev.*, **129**, 550–560.
- , and S. J. Colucci, 1997: Verification of Eta-RSM short-range ensemble forecasts. *Mon. Wea. Rev.*, **125**, 1312–1327.
- Harrison, M., T. Palmer, D. Richardson, and R. Buizza, 1999: Analysis and model dependencies in medium-range ensembles: Two transplant case studies. *Quart. J. Roy. Meteor. Soc.*, **125**, 2487–2515.
- Holton, J. R., 1979: *An Introduction to Dynamic Meteorology*. 2d ed. Academic Press, 391 pp.
- Hou, D., E. Kalnay, and K. K. Drogemeier, 2001: Objective verification of the SAMEX '98 ensemble forecasts. *Mon. Wea. Rev.*, **129**, 73–91.
- Laprise, R., 2003: Resolved scales and nonlinear interactions in limited-area models. *J. Atmos. Sci.*, **60**, 768–779.
- , M. R. Varma, B. Denis, D. Caya, and I. Zawadzki, 2000: Predictability of a nested limited-area model. *Mon. Wea. Rev.*, **128**, 4149–4154.
- Leith, C. E., 1971: Atmospheric predictability and two-dimensional turbulence. *J. Atmos. Sci.*, **28**, 145–161.
- , 1974: Theoretical skill of Monte Carlo forecasts. *Mon. Wea. Rev.*, **102**, 409–418.
- , and R. H. Kraichnan, 1972: Predictability of turbulent flows. *J. Atmos. Sci.*, **29**, 1041–1058.
- Lilly, D. K., 1984: Some facets of the predictability problem for atmospheric mesoscales. *Predictability of Fluid Motions*, G. Holloway and B. J. West, Eds., American Institute of Physics, 287–294.
- Lorenz, E. N., 1963: Deterministic nonperiodic flow. *J. Atmos. Sci.*, **20**, 131–140.
- , 1969a: Atmospheric predictability as revealed by naturally occurring analogues. *J. Atmos. Sci.*, **26**, 636–646.
- , 1969b: The predictability of a flow which possesses many scales of motion. *Tellus*, **21**, 289–307.

- , 1969c: Three approaches to atmospheric predictability. *Bull. Amer. Meteor. Soc.*, **50**, 345–349.
- , 1982: Atmospheric predictability experiments with a large numerical model. *Tellus*, **34**, 505–513.
- , 1984: Estimates of atmospheric predictability at medium range. *Predictability of Fluid Motions*, G. Holloway and B. J. West, Eds., American Institute of Physics, 133–140.
- Nutter, P., 2003: Effects of nesting frequency and lateral boundary perturbations on the dispersion of limited-area ensemble forecasts. Ph.D. dissertation, University of Oklahoma, 156 pp.
- , M. Xue, and D. Stensrud, 2004: Application of lateral boundary condition perturbations to help restore dispersion in limited-area ensemble forecasts. *Mon. Wea. Rev.*, **132**, 2378–2390.
- Orrell, D., L. Smith, J. Barkmeijer, and T. Palmer, 2001: Model error in weather forecasting. *Nonlinear Proc. Geophys.*, **8**, 357–371.
- Paegle, J., Q. Yang, and M. Wang, 1997: Predictability in limited area and global models. *Meteor. Atmos. Phys.*, **63**, 53–69.
- Reynolds, C. A., P. J. Webster, and E. Kalnay, 1994: Random error growth in NMC's global forecasts. *Mon. Wea. Rev.*, **122**, 1281–1305.
- Schubert, S. D., and M. Suarez, 1989: Dynamical predictability in simple general circulation model: Average error growth. *J. Atmos. Sci.*, **46**, 353–370.
- Smagorinsky, J., 1969: Problems and promises of deterministic extended range forecasting. *Bull. Amer. Meteor. Soc.*, **50**, 286–311.
- Stephenson, D. B., and F. J. Doblas-Reyes, 2000: Statistical methods for interpreting Monte Carlo ensemble forecasts. *Tellus*, **52A**, 300–322.
- Tennekes, H., 1978: Turbulent flow in two- and three-dimensions. *Bull. Amer. Meteor. Soc.*, **59**, 22–28.
- Thompson, P. D., 1957: Uncertainty of initial state as a factor in the predictability of large-scale atmospheric flow patterns. *Tellus*, **9**, 275–295.
- , 1984: A review of the predictability problem. *Predictability of Fluid Motions*, G. Holloway and B. J. West, Eds., American Institute of Physics, 1–10.
- Toth, Z., E. Kalnay, S. M. Tracton, R. Wobus, and J. Irwin, 1997: A synoptic evaluation of the NCEP ensemble. *Wea. Forecasting*, **12**, 140–153.
- Van Tuyl, A. H., and R. M. Errico, 1989: Scale interaction and predictability in a mesoscale model. *Mon. Wea. Rev.*, **117**, 495–517.
- Vukicevic, T., and J. Paegle, 1989: The influence of one-way interacting lateral boundary conditions on predictability of flow in bounded numerical models. *Mon. Wea. Rev.*, **117**, 340–350.
- , and R. M. Errico, 1990: The influence of artificial and physical factors upon predictability estimates using a complex limited-area model. *Mon. Wea. Rev.*, **118**, 1460–1482.
- Wandishin, M. L., S. L. Mullen, D. J. Stensrud, and H. E. Brooks, 2001: Evaluation of a short-range multimodel ensemble system. *Mon. Wea. Rev.*, **129**, 729–747.
- Warner, T. T., L. E. Key, and A. M. Lario, 1989: Sensitivity of mesoscale-model forecast skill to some initial-data characteristics, data density, data position, analysis procedure and measurement error. *Mon. Wea. Rev.*, **117**, 1281–1310.
- , R. A. Peterson, and R. E. Treadon, 1997: A tutorial on lateral boundary conditions as a basic and potentially serious limitation to regional numerical weather prediction. *Bull. Amer. Meteor. Soc.*, **78**, 2599–2617.
- Xue, M., 2000: High-order monotonic numerical diffusion and smoothing. *Mon. Wea. Rev.*, **128**, 2853–2864.